

# Photon Number-Resolving Quantum Reservoir Computing

Sam Nerenberg,<sup>1,\*</sup> Oliver Neill,<sup>1,\*</sup> Giulia Marcucci,<sup>1</sup> and Daniele Faccio<sup>1</sup>

<sup>1</sup>*Department of Physics and Astronomy, University of Glasgow, Glasgow G12 8QQ, UK.*

Neuromorphic processors improve the efficiency of machine learning algorithms through the implementation of physical artificial neurons to perform computations. However, whilst efficient classical neuromorphic processors have been demonstrated in various forms, practical quantum neuromorphic platforms are still in the early stages of development. Here we propose a fixed optical network for photonic quantum reservoir computing that is enabled by photon number-resolved detection of the output states. This significantly reduces the required complexity of the input quantum states while still accessing a high-dimensional Hilbert space. The approach is implementable with currently available technology and lowers the barrier to entry to quantum machine learning.

**Introduction.** Quantum machine learning (QML) is a broad field in which the physical features of quantum systems are leveraged to process data [1]. In addition to promising speedups for classical tasks, QML systems are able to directly process quantum data leading to improvements in existing methods of extracting and manipulating quantum information [2, 3]. Quantum neural networks (QNNs) are a subclass of QML in which the structure of artificial neural networks (ANNs) is composed of linked quantum states which, together with their interactions, may be parametrized and trained. Generally, these algorithms are implemented on quantum computers, the most promising of which use either superconducting qubits or squeezed states of light as their substrate. Although these devices show great promise to scale thanks to years of hard efforts [4–9], the technology is out of reach for most laboratories and may indeed be overkill for many routine data processing tasks. This opens a door for neuromorphic hardware that can be specialized to various analysis tasks on classical or quantum data with minimal experimental overhead. Among the different hardware implementations of QNNs, linear photonic networks (LPNs) are of particular interest for reasons including: room-temperature operation, low power consumption, convenience of networking devices and scalability [10]. In addition, LPNs have a rich theoretical framework in place and have already been used to demonstrate forms of quantum computation [4, 5, 11–16]. These results are promising in the context of a search for more efficient neuromorphic systems. Indeed, all approaches that require training of a large number of degrees of freedom come at significant computational and environmental costs, which are major motivations to develop optical ANNs [17].

Reservoir computing (RC) is a particular sub-class of ANNs that have attracted attention as a viable and efficient neuromorphic platform. Characterized by its unique strategy of combining the collective hidden layers of an ANN into a single, random, high-dimensional layer with fixed dynamics, RC significantly mitigates the computational load typically associated with extensive

ANN training. This is achieved by performing training solely at the readout stage. Implemented in LPNs, RC leverages the intrinsic complexity and high-dimensional state space generated by the platform. Coupled with the innate parallel processing strength and growth potential of LPNs, RC presents a compelling model for the future of large-scale and high-speed computing.

Here, we present the concept of photon number-resolving quantum reservoir computing (Photon-QuaRC). This is a quantum reservoir computer (QRC) based on a linear photonic network in which information is encoded and manipulated in the polarisation states of light. We improve computational power without increasing network complexity by applying photon number-resolved detection at the output. This is made possible through the combinatorial scaling of the output Hilbert space with the number of input photons. Furthermore, we show that we can retain the advantage gained through quantum multiphoton interference inside the network without having to prepare large photon-number Fock states. The reservoir architecture allows implementation in a wide range of simple physical systems such as multimode fibers or scattering materials [18, 19]. It also avoids the need to optimize the network and reduces all training energy costs to a matrix inversion. Due to these features, we present our method as a practical path towards versatile, scalable quantum machine learning.

**Polarising linear optical networks as quantum reservoirs.** Various forms of reservoir computers (RCs) have been studied extensively as they provide a framework for neural networks that can be naturally mapped to the dynamics of physical systems [20] including squeezed light in a circulating nonlinear cavity [21]. Several systems have been based on random optical media [19, 21] - we show that these can indeed be extended to QRCs based on a general BosonSampling scheme. Figure 1(a) shows the schematic layout of Photon-QuaRC:  $N$  photons are fed into the physical system which is composed of two sequential  $M$ -port LPNs: the encoding layer,  $E(x)$  which operates only on the polarisation degree of freedom of the input state and the reservoir,  $R$

which couples both spatial and polarisation modes. Encoding follows trajectories on a Poincaré sphere, schematically indicated in the figure. The output then consists of Fock state distributions  $F(x)$  that we can then use to solve the task of interpolating generic functions,  $f(x)$ . This is achieved with a training phase, outlined in Fig. 1(b) where the weights  $W$  are learned and then used in the inference phase, Fig. 1(c) to perform machine learning tasks, e.g. function interpolation. We now provide more details for each of these steps.

**Quantum reservoir computer output.** For input data  $x$  the output of the QRC is

$$\langle \vec{F}(x) \rangle = \langle \vec{n}^{in} \mathcal{E}^\dagger(x) \mathcal{R}^\dagger | \vec{F} | \mathcal{R} \mathcal{E}(x) \vec{n}^{in} \rangle, \quad (1)$$

where  $\mathcal{R}$  and  $\mathcal{E}(x)$  are the unitary Fock space scattering matrices corresponding to the reservoir and encoding transformations, respectively. These may be built from the mode-coupling matrices of the corresponding LPNs as shown in Ref. [22].  $\langle \vec{F}(x) \rangle$  denotes the probability distribution over the  $d = \binom{N+M-1}{N}$  measurement outcomes at the reservoir output, and  $|\vec{n}^{in}\rangle$  is the input Fock state, prior to the encoding. The scaling of  $d$  with  $N$  is a key feature of the BosonSampling approach as it allows us to expand the feature space combinatorially faster than the physical network complexity.

The target function is approximated from the reservoir output by a matrix multiplication

$$\vec{f}(x) = W \langle \vec{F}(x) \rangle, \quad (2)$$

where  $W$  is the weight matrix learned from linear regression on labelled data.

Prior BosonSampling-inspired approaches to QML use networks made of trainable blocks that are tuned to produce a desired target function [23]. However, a key feature of the Photon-QuaRC architecture is that the target function is computed without having to optimize over the network parameters.

**Fourier space feature learning.** Previous work has shown that the output of any quantum neural network can be expressed as a partial Fourier series of the data [23–25]. This output  $g(x)$  can be written as

$$g(x) = \sum_{\omega \in \Omega_n} c_\omega e^{i\omega x}, \quad (3)$$

where  $\Omega_n$  is the set of all unique frequencies that the network can generate. Frequencies  $\omega \in \Omega_n$  are determined by the encoding scheme and the number of input photons, while the coefficients  $c_\omega$  are fixed by the network structure. The properties of  $\Omega_n$  (size, center and maximum frequency) determine the class of functions that the network can approximate, a.k.a. *expressivity*. However, while  $\Omega_n$  contains information about the ability of

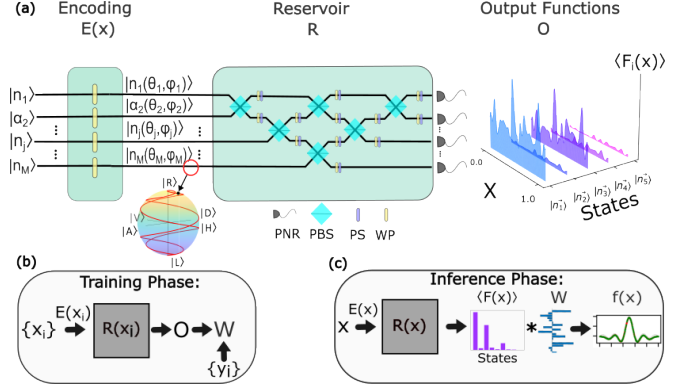


FIG. 1. **Photon-QuaRC schematic overview.** (a) Horizontally polarised Fock and coherent states in  $M$  different spatial modes are directed into an encoding block  $E(x)$  that encodes the input data,  $x$ , in a multimode polarisation state. The polarisation at each port is parametrized on the Poincaré Sphere by  $\theta_m$  and  $\phi_m$ , which are the azimuth and zenith angles, respectively. This state is fed into a random, fixed linear optical network built from polarising beam splitters (PBS), waveplates (WP) and phase shifters (PS). Output states are subject to polarisation-independent measurement by photon number-resolving (PNR) detectors. Approximation of the Fock state distribution  $\langle \vec{F}(x) \rangle$  by repeated sampling constitutes the device output, Eq. (1). (b) During the training stage, labelled data  $\{x_i\}$  are encoded, and the reservoir outputs are saved in an array  $O$ . The elements of this array are then fit to labels  $\{y_i\}$  to learn weights,  $W$ . (c) In the inference phase the target function  $\vec{f}(x)$  on input data is evaluated by multiplying  $\langle \vec{F}(x) \rangle$  by  $W$ , Eq. (2).

a given design to specialize to a task, it does not provide a characterization of the robustness under operation, as we discuss below.

A primary challenge in scaling the feature space in QML using optical systems is generating large-photon-number Fock states, which can be prohibitive in practice. While these high-photon-number states offer optimal performance within certain constraints, it prompts us to consider whether comparable results can be achieved with fewer quantum resources. For example, prior work has shown that by leveraging the interference between a single-photon Fock state and a coherent state, one can create quantum mechanical states with arbitrary photon numbers [26, 27]. This approach also requires photon number-resolving detection and post-selection, so as to distill quantum interference of the desired order from the output.

We adopt this concept and therefore start from a general state that combines coherent and Fock components in a unified form,

$$|\psi_{\vec{\alpha}, \vec{n}}\rangle = \prod_{m=1}^M e^{\alpha_m a_m^\dagger - \alpha_m^* a_m} \frac{(a_m^\dagger)^{n_m}}{\sqrt{n_m!}} |0\rangle, \quad (4)$$

where  $\alpha_m$  and  $n_m$  are the coherent state amplitude and number of added photons in mode  $m$  respectively. If the

$\alpha_m$  or  $n_m$  are set to zero, Eq. (4) simplifies to the standard form of a Fock state or a coherent state, respectively. Any state with non-zero  $n_m$  and  $\alpha_m$  is referred to as a hybrid state. In what follows we will notate a Hybrid state as  $|\psi_{\vec{\alpha},\vec{n}}\rangle = |\alpha_1 + n_1, \dots, \alpha_m + n_m\rangle$  (see SM for more details).

**Model of polarising network.** We construct the network adapting the method proposed by Reck *et al.* [28] with some key modifications: we replace each spatial mode with a pair of corresponding polarisation modes and the constituent optical elements are polarising beam-splitters, arbitrary birefringent waveplates and phase shifters. The full network then couples 2M modes, and the primitive elements operate on 4x4 subspaces (see the SM for details).

The input to the QRC is a fixed state which is encoded with the data and scattered into a superposition of Fock states at the output. To describe the action of the encoding layer at each input port we apply the ladder operator replacement rule

$$a_m^\dagger \rightarrow \cos \theta_m(x) a_{m,H}^\dagger + \sin \theta_m(x) e^{i\phi_m(x)} a_{m,V}^\dagger, \quad (5)$$

where  $a_m^\dagger$  is a creation operator acting on port  $m$  and  $a_{m,H/V}^\dagger$  denotes a creation operator acting on the  $H/V$  polarised component of port  $m$ . Thus, each data point is encoded as a set of Stokes vectors by waveplates at each input port. A given encoding scheme consists of a joint trajectory on the Poincaré sphere parameterized by the data. As the input state traverses this trajectory the probability of each output state follows a smooth curve on the sphere. These output functions are the basis elements which are combined in Eq. (2) to perform a given computational task, e.g. approximate a target function.

**Performance measures.** The QRC performance on any task is determined by the set of linearly independent observable functions it can generate and whether they can be feasibly detected above noise. We therefore introduce additional performance measures beyond the Fourier spectrum to better quantify expressivity.

*Output matrix rank:* During the training phase, labelled data is fed into the network and the reservoir output is stored in an array  $O_{ij} = \langle F_i(x_j) \rangle$ . The Gram matrix  $O^\dagger O$  then contains all inner products between output function pairs and its rank determines the number of unique basis functions that span the output space. Although the output functions contained in  $O$  can be mapped to the elements of Eq. (3) using a Fourier transform, the advantage of using  $\text{rank}(O^\dagger O)$  as a performance metric is that it counts the dimension of the space spanned by the observables rather than the number of frequencies in the output. This also implies that, in order to be fully expressive, a network must output at least as many observables as the number of frequency components it can

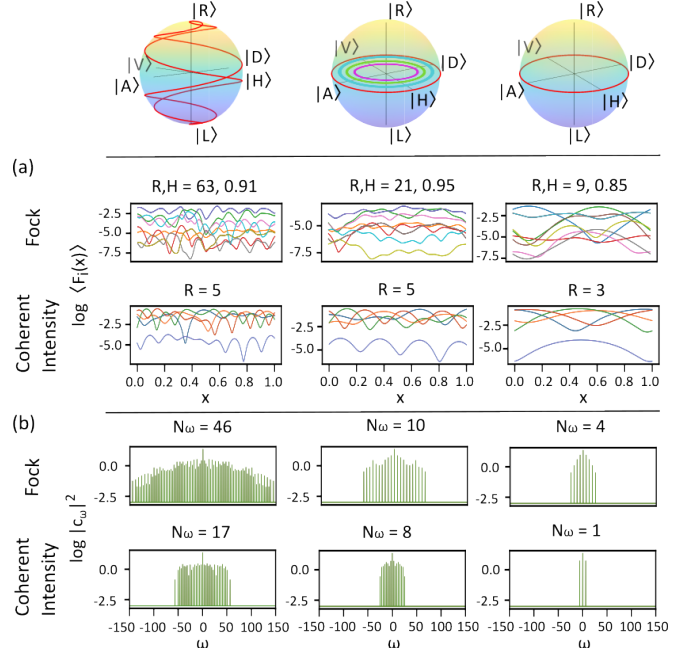


FIG. 2. **Photon-QuaRC, quantum and classical behavior for various encodings.** Two different states and detection schemes are applied to the same  $M = 5$  network. **Fock:** A four-photon Fock state  $|\vec{n}\rangle = |1, 1, 1, 1, 0\rangle$  with perfect PNR detection. **Coherent Intensity:** A four-port classical state  $|\vec{\alpha}\rangle = |.5, .5, .5, .5, 0\rangle$  with intensity detection at each port. **(a)** The first 10 most probable output functions for each case. **(b)** Corresponding Fourier spectra for each set of output functions. Each column corresponds to a different encoding scheme. **Left:** Spiral with  $l_m = 4m$ . **Center:** Multi-linear where  $l_m = m$ . **Right:** Uniform-linear. The labels  $R$  and  $H$  refer to the rank and spectral entropy of the distribution respectively.  $N_\omega$  denotes the number of elements in a spectrum excluding redundant negative frequencies and the DC component.

generate.

*Spectral entropy:* In a realistic scenario  $\langle \vec{F}(x) \rangle$  must be approximated by sampling with imperfect detectors. Because of its non-uniformity, some basis functions will not be accessible with a practical fixed number of samples, thus reducing the output's effective rank. To account for this we define the spectral entropy based on recent studies in complex networks [29]

$$H = - \sum_i \sigma_i \log_2 \sigma_i, \quad (6)$$

where  $\{\sigma_i\}$  is the normalized singular value spectrum of the matrix  $O^\dagger O$  and relates to the relative frequencies of output basis elements.

**Encoding schemes.** The expressive power of a network is determined by the encoding scheme and the input state. While an exhaustive investigation of all possible encodings and input states is outside the scope of this work, we will discuss a few schemes here, also shown in the top row of Fig. 2 (see the SM for more details).

*Uniform linear:* The first and simplest encoding is one in which all photons are given the same linear polarisation angle  $\theta \in [0, 2\pi]$  which traverses one equatorial orbit over the data domain,  $\theta = lx$ .

*Multi-slope linear:* As the uniform linear scheme is ultimately limited by the number of photons, it is natural to try to broaden the spectrum by encoding multiple frequencies directly in each port. One method is to apply a different linear function to the polarisation of each photon  $\theta_m = l_m x$ .

*Spiral:* By including elliptical polarisations such that our data are encoded in both  $\theta$  and  $\phi$  in Eq. (5) we can design encodings with useful properties inherited from the topology of the Poincaré sphere. A natural geometry is a spiral which traverses the sphere from pole to pole and returns to form a closed curve. This encoding can undergo an arbitrary number of azimuthal revolutions  $l_m$  over the domain of the data while also providing low-frequency content from the zenith traversal.

Figure 2 displays the output functions and frequency spectrum generated by several different encoding schemes for both a four photon Fock state with PNR detection as well as a four port coherent state with intensity detection. We can see that the choice of encoding can tune the rank, distribution and spectrum of the output. In the Fock case we can see that adding complexity to the encoding trajectory increases the size of the Fourier spectrum as well as the rank and spectral entropy of the output. This in turn, improves the expressivity of the system. In contrast, the rank of the classical case - coherent states with intensity detection - is limited to the number of output ports of the network and the Fourier spectrum grows much slower. This further serves to illustrate the scaling advantages gained through quantum resources. The change in frequency content with different encodings is evident in the curvature of the output functions in Fig. 2a where the spiral and multi-linear encodings bias the most probable functions to higher frequencies. It is important to note that choosing an encoding scheme which simply maximizes rank does not ensure optimal performance on a task. Encodings must be chosen in a principled manner to balance rank, spectral entropy, and frequency content based on the desired task.

**Photon-QuaRC as a function interpolator.** In Fig. 3 we demonstrate differences in performance between various implementations applied to machine learning tasks, e.g. function interpolation. The ultimate goal is to maximize performance for a fixed number of resources and to demonstrate each design under realistic conditions of operation.

We first define the target function  $f^*(x)$  on an interval  $x$ , and discretize it to generate sets of data and labels,  $\{x_i, y_i\}$ . These are randomly and uniformly split into two

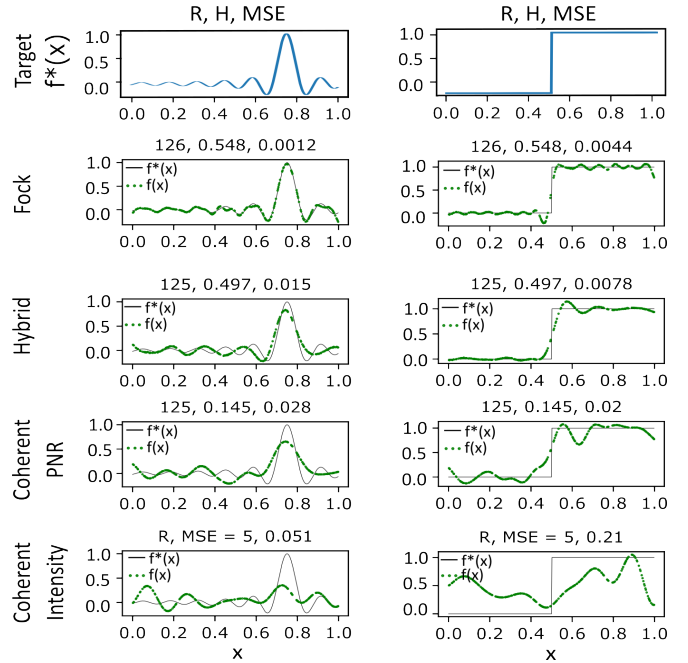


FIG. 3. **Function interpolation**, comparing the approximation  $f(x)$  to the target function  $f^*(x)$ . All trials use spiral encoding with  $l_m = 3m$  and post-selection on  $\leq 4$  photon events with  $\eta = .9$  and  $N_{\text{samp}} = 10^7$ . Performance metrics [R,H,MSE] are listed in the title for each task/state combination. The states used are **Fock**:  $|\vec{n}\rangle = |1, 1, 1, 1, 0\rangle$  with PNR detection, **Hybrid**:  $|\psi_{\vec{\alpha}, \vec{n}}\rangle = |0.5+1, 0.5+1, 0, 0, 0\rangle$  with PNR detection, **Coherent PNR**:  $|\vec{\alpha}\rangle = |0.5, 0.5, 0, 0, 0\rangle$  with PNR detection, **Coherent Intensity**: Fully classical operation using  $|\vec{\alpha}\rangle = |0.5, 0.5, 0.5, 0.5, 0\rangle$  with intensity detection. Each coherent state subject to PNR detection is approximated as a superposition of Fock states up to the sixth order. Each trial uses a 50/50 test/train data split.

sets for training and validation, such that the device must learn the entire function in order to correctly interpolate it.

To simulate the output in real-world scenarios, accounting for limited sampling and imperfect detection, we employ a binomial model with a detector efficiency  $\eta$ . This model is applied to the ideal distribution  $\langle \vec{F}(x) \rangle$ . We then post-select the Fock subspace that corresponds to the detection events of interest while all other events are grouped into a non-detection state. After determining the final distribution, we draw a total number of samples  $N_{\text{samp}}$  to simulate the process of injecting copies of the input state to build statistics. The training data are used to form the output matrix  $O$  from which we extract the rank and spectral entropy. We then inject the validation data and apply a mean squared error (MSE) between the outputs and their corresponding labels to quantify the task performance.

**Results.** As shown in Fig. 3, there exists a clear improvement in performance and generalization as we increase the quantum resources. The details of this hierar-

chy for a specific function depend on the overlap of the output and target spectra. However, the correlation of MSE to the spectral entropy across vastly different target functions suggests that increasingly quantum sources are more robust under realistic conditions of operation due to higher uniformity in the output distribution over singular values (see SM for more details). We can see that the Fock state input yields the lowest error for both the sinc and step function interpolation. This is because the definite photon number ensures that the four-photon amplitudes in  $\langle \vec{F}(x) \rangle$  are most probable and well-sampled. The hybrid states display better performance and generalization across tasks relative to the coherent states for similar reasons as the addition of the single photons reduces the uncertainty in photon number. However, as the higher-photon terms are less probable than with Fock states, hybrid states display a larger MSE for each task. Beyond the clear increase in performance with quantum resources at the input, we also note that in all cases we see an increase in performance related to photon number-resolving detection at the output: this alone grants an advantage over the fully classical case (i.e. coherent states sampled without PNR detection) due to the scaling of the output space. A discussion of how particular states were chosen for comparison may be found in the SM.

**Conclusions.** We have presented an approach to QML that is based on a linear photonic network. This shows an advantage when using quantum resources, with PNR detection as the minimal quantum resource which alone yields improvement over the tested classical measurements. Beyond the use of PNR, we also show a further hierarchical improvement of the QRC with increasing quantum resources at the input where performance increases from coherent to hybrid to pure Fock states. The reservoir architecture allows the device to be re-aliased with simple optical systems, such as multimode fibers, and saves time and energy in the training stage. In this work we demonstrated the performance for function interpolation. Although it can also be used for classification, we feel that the method is best suited to tasks in which data encoded in quantum states are mapped to functions of a small number of variables. One example would be as integrated quantum information processing units in communication networks performing tasks such as quantum state tomography. Future work will focus on developing further optimized encoding schemes and design alterations to allow for time-series prediction.

019-0149-8 (2019).

- [3] H.-Y. Huang, M. Broughton, J. Cotler, S. Chen, J. Li, M. Mohseni, H. Neven, R. Babbush, R. Kueng, J. Preskill, and J. R. McClean, *Science* **17**, 2023.
- [4] H. Wang, J. Qin, X. Ding, M. C. Chen, S. Chen, X. You, Y. M. He, X. Jiang, L. You, Z. Wang, C. Schneider, J. J. Renema, S. Höfling, C. Y. Lu, and J. W. Pan, *Physical Review Letters* **123**, 10.1103/PhysRevLett.123.250503 (2019).
- [5] L. S. Madsen, F. Laudenbach, M. F. Askarani, F. Rortais, T. Vincent, J. F. Bulmer, F. M. Miatto, L. Neuhaus, L. G. Helt, M. J. Collins, A. E. Lita, T. Gerrits, S. W. Nam, V. D. Vaidya, M. Menotti, I. Dhand, Z. Vernon, N. Quesada, and J. Lavoie, *Nature* **606**, 75 (2022).
- [6] J. M. Arrazola, V. Bergholm, K. Brádler, T. R. Bromley, M. J. Collins, I. Dhand, A. Fumagalli, T. Gerrits, A. Goussev, L. G. Helt, J. Hundal, T. Isacsson, R. B. Israel, J. Izaac, S. Jahangiri, R. Janik, N. Killoran, S. P. Kumar, J. Lavoie, A. E. Lita, D. H. Mahler, M. Menotti, B. Morrison, S. W. Nam, L. Neuhaus, H. Y. Qi, N. Quesada, A. Repington, K. K. Sabapathy, M. Schuld, D. Su, J. Swinerton, A. Száva, K. Tan, P. Tan, V. D. Vaidya, Z. Vernon, Z. Zabaneh, and Y. Zhang, *Nature* **591**, 54 (2021).
- [7] W. Bogaerts, D. Pérez, J. Capmany, D. A. Miller, J. Poon, D. Englund, F. Morichetti, and A. Melloni, *Programmable photonic circuits* (2020).
- [8] W. Luo, L. Cao, Y. Shi, L. Wan, H. Zhang, S. Li, G. Chen, Y. Li, S. Li, Y. Wang, S. Sun, M. F. Karim, H. Cai, L. C. Kwek, and A. Q. Liu, *Recent progress in quantum photonic chips for quantum communication and internet* (2023).
- [9] M. Kjaergaard, M. E. Schwartz, J. Braumüller, P. Krantz, J. I.-J. Wang, S. Gustavsson, and W. D. Oliver, *Annual Review of Condensed Matter Physics* **11**, 369 (2020), <https://doi.org/10.1146/annurev-conmatphys-031119-050605>.
- [10] P. L. McMahon 10.1038/s42254-023-00645-5 (2023).
- [11] S. H. Tan and P. P. Rohde, *The resurgence of the linear optics quantum interferometer — recent advances and applications* (2019).
- [12] B. T. Gard, K. R. Motes, J. P. Olson, P. P. Rohde, and J. P. Dowling doi:10.1142/9789814678704\_0008 (2014).
- [13] S. S. Paivi Torma and I. Jex, *Physical Review A* **52**, 10.1103/physreva.52.4853 (1995).
- [14] R. van der Meer, S. Huber, P. W. H. Pinkse, R. García-Patrón, and J. J. Renema, (2021).
- [15] M. A. Broome, A. Fedrizzi, S. Rahimi-Keshari, J. Dove, S. Aaronson, T. C. Ralph, and A. G. White, *Science* **339**, 794 (2013).
- [16] G. Marcucci, D. Pierangeli, P. W. H. Pinkse, M. Malik, and C. Conti, *Opt. Express* **28**, 14018 (2020).
- [17] D. Wright, C. Igel, G. Samuel, and R. Selvan, (2023).
- [18] H. Defienne, M. Barbieri, I. A. Walmsley, B. J. Smith, and S. Gigan, *Science Advances* **2**, 10.1126/sciadv.1501054 (2016).
- [19] M. Rafayelyan, J. Dong, Y. Tan, F. Krzakala, and S. Gigan, *Physical Review X* **10**, 10.1103/PhysRevX.10.041037 (2020).
- [20] G. Tanaka, T. Yamane, J. B. Héroux, R. Nakane, N. Kanazawa, S. Takeda, H. Numata, D. Nakano, and A. Hirose, *Neural Networks* **115**, 100 (2019).
- [21] J. García-Beni, G. L. Giorgi, M. C. Soriano, and R. Zambrini 10.1103/PhysRevApplied.20.014051 (2022).

\* These authors contributed equally to this work

- [1] J. Biamonte, P. Wittek, N. Pancotti, P. Rebentrost, N. Wiebe, and S. Lloyd, *Nature* **549**, 195 (2017).
- [2] S. Ghosh, A. Opala, M. Matuszewski, T. Paterek, and T. C. Liew, *npj Quantum Information* **5**, 10.1038/s41534-

- [22] S. Scheel, Permanents in linear optical networks (2004), arXiv:quant-ph/0406127 [quant-ph].
- [23] B. Y. Gan, D. Leykam, and D. G. Angelakis, EPJ Quantum Technology **9**, 10.1140/epjqt/s40507-022-00135-0 (2022).
- [24] M. Schuld, R. Sweke, and J. J. Meyer, Physical Review A **103**, 10.1103/PhysRevA.103.032430 (2021).
- [25] F. J. G. Vidal and D. O. Theis, Frontiers in Physics **8**, 10.3389/fphy.2020.00297 (2020).
- [26] I. Afek, O. Ambar, and Y. Silberberg, Science **328**, 879 (2010), <https://www.science.org/doi/pdf/10.1126/science.1188172>.
- [27] A. Windhager, M. Suda, C. Pacher, M. Peev, and A. Poppe 10.1016/j.optcom.2010.12.019 (2010).
- [28] M. Reck, A. Zeilinger, H. J. Bernstein, and P. Bertani, Experimental realization of any discrete unitary operator (1994).
- [29] V. Thibeault, A. Allard, and P. Desrosiers, Nature Physics 10.1038/s41567-023-02303-0 (2024).

# Photon Number-Resolving Quantum Reservoir Computing

## Supplementary Material

Sam Nerenberg,<sup>1,\*</sup> Oliver Neill,<sup>1,\*</sup> Giulia Marcucci,<sup>1</sup> and Daniele Faccio<sup>1</sup>

<sup>1</sup>*Department of Physics and Astronomy, University of Glasgow, Glasgow G12 8QQ, UK.*

(Dated: February 12, 2024)

### REPRESENTATION OF FOCK STATES OF POLARISED PHOTONS

We can write a Fock state for a device with  $M$  ports and  $N$  photons - each with polarisation state  $(\theta_k, \phi_k)$  in Poincare sphere coordinates as

$$|\vec{n}(\vec{\theta}, \vec{\phi})\rangle = \prod_{m=1}^M \frac{\prod_{k=1}^{n_m} a_m^\dagger(\theta_k, \phi_k)}{\sqrt{n_m!}} |0\rangle, \quad (1)$$

where  $a_m^\dagger(\theta_k, \phi_k)$  is a creation operator acting on port  $m$  imparting an internal state  $k$ , and  $n_m$  is the number of photons in port  $m$  such that  $\sum_{m=1}^M n_m = N$ . The outer product runs over the ports and the inner one applies the appropriate creation operators at that port. For simplicity as well as experimental practicality we will assume that all photons launched into the same input port have the same polarisation state. Eq. 1 then simplifies to

$$|\vec{n}(\vec{\theta}, \vec{\phi})\rangle = \prod_{m=1}^M \frac{a_m^\dagger(\theta_m, \phi_m)^{n_m}}{\sqrt{n_m!}} |0\rangle. \quad (2)$$

To represent the polarisation state explicitly in terms of the  $(\theta_m, \phi_m)$  we write the state of the input or output in the  $2M$  mode occupation number basis. In this representation, each of the  $M$  ports has two associated modes representing the horizontally and vertically polarised components of the electric field. By applying the creation operator replacement rule  $a_m^\dagger(\theta_m, \phi_m)^{n_m} \rightarrow \cos \theta_m a_{m,H}^\dagger + \sin \theta_m e^{i\phi_m} a_{m,V}^\dagger$  the state of the field can be written like

$$|\vec{n}(\vec{\theta}, \vec{\phi})\rangle = \prod_{m=1}^M \frac{(\cos \theta_m a_{m,H}^\dagger + \sin \theta_m e^{i\phi_m} a_{m,V}^\dagger)^{n_m}}{\sqrt{n_m!}} |0\rangle, \quad (3)$$

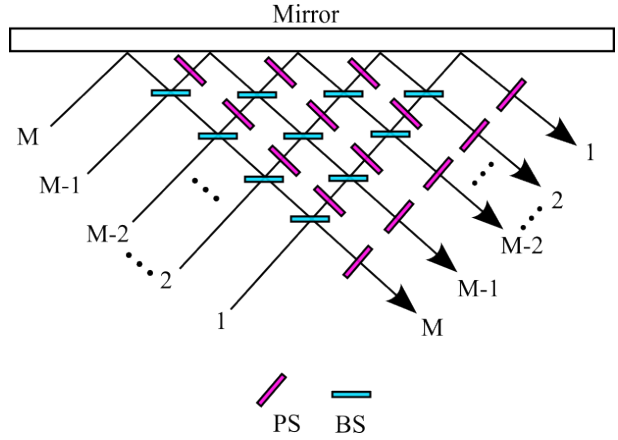
where  $a_{m,H/V}^\dagger$  denotes a creation operator acting on the horizontally/vertically polarised component of port  $m$ . The coefficients of these operators may be converted to Poincare sphere coordinates.

### MODEL OF POLARISING NETWORK

Quantum states of light may be propagated through a linear optical network (LON) by applying the methods developed by Scheel or Huertel et al. [? ?]. These methods take as input the unitary scattering matrix  $\Lambda$

whose elements are the coupling amplitudes from each input mode to each output mode of the LON.

Without loss of generality, we construct a LON using the design of Reck et al. as shown in Supplementary Figure 1. It is composed of a triangular arrangement of  $Z = M(M-1)/2$  beamsplitters and  $M(M+1)/2$  phase-shifters. Such a network, if lossless, can physically realize any discrete  $M \times M$  unitary transform [?].



Supplementary Figure 1.  $M$ -port LON using triangular arrangement of beamsplitters (BS) and phase shifters (PS).

The  $\Lambda$  matrix is built from the ordered product of beamsplitter matrices which represent the coupling between two spatial modes at the crossing points of the interferometer. A single lossless beamsplitter followed by a phase shifter may be represented by a unitary matrix with two free parameters as follows:

$$C(\alpha, \beta) = \begin{pmatrix} \cos \alpha e^{i\beta} & \sin \alpha \\ -\sin \alpha e^{i\beta} & \cos \alpha \end{pmatrix}, \quad (4)$$

where  $\cos \alpha = t$  and  $\sin \alpha = r$  are the transmission and reflectance coefficients of the beamsplitter and  $\beta$  is the phase accrued after propagation through the phase-shifter. To apply this rotation in an  $M$ -dimensional space, we use the method of Givens rotations and embed the two-dimensional rotation in an  $M \times M$  identity matrix so that it operates only in the appropriate two-dimensional subspace. The Givens rotation corresponding to a beamsplitter/phase-shifter combination operat-

ing on modes  $i$  and  $j$  may be written as

$$\lambda^{ij}(\alpha, \beta) = g^{ij}(C)$$

$$= \begin{pmatrix} 1 & & \dots & & 0 \\ \vdots & \lambda_{ij} = C_{11} & & \lambda_{i,i+j} = C_{12} & \vdots \\ & & 1 & & \vdots \\ & \lambda_{i+j,j} = C_{21} & & \lambda_{j,j} = C_{22} & 1 \\ 0 & & \dots & & \end{pmatrix}, \quad (5)$$

where we use  $g^{ij}(C)$  to denote the Givens rotation generated from the matrix  $C$ . Next, we define a diagonal matrix,  $\Psi$  whose entries contain the final output phase shifts for each mode:

$$\Psi = \begin{pmatrix} e^{i\psi_1} & 0 & \dots & 0 \\ 0 & e^{i\psi_2} & \dots & 0 \\ \vdots & & \ddots & \vdots \\ 0 & 0 & \dots & e^{i\psi_M} \end{pmatrix}. \quad (6)$$

The full unitary transformation in the space of modes,  $\Lambda$  is built by an ordered product of  $Z$  two-mode coupling matrices followed by  $\Psi$  as follows:

$$\Lambda = \Psi [\lambda^{M-1,M}] [\lambda^{M-2,M-1} \lambda^{M-2,M}] \dots \dots [\lambda^{1,2} \lambda^{1,3} \dots \lambda^{1,M-1} \lambda^{1,M}], \quad (7)$$

where ordering is determined by the labeling of modes in Fig. 1.

To model a polarising linear optical network (PLON) we construct  $\Lambda$  in the  $2M$  dimensional space formed from the tensor product of the state space of  $M$  spatial modes with the 2-dimensional state space of polarisation. We follow the same procedure as before, however, the primitive elements are now imperfect polarising beamsplitters, birefringent crystals and phase shifters operating in the tensor product space. The  $4 \times 4$  matrices defining these transformations are:

$$\text{IPBS} = \begin{pmatrix} m_H & p_H & m_V & p_V \\ \cos \alpha_h & \sin \alpha_h & 0 & 0 \\ -\sin \alpha_h & \cos \alpha_h & 0 & 0 \\ 0 & 0 & \cos \alpha_v & \sin \alpha_v \\ 0 & 0 & -\sin \alpha_v & \cos \alpha_v \end{pmatrix} \begin{matrix} m_H \\ p_H \\ m_V \\ p_V \end{matrix}, \quad (8)$$

where  $\alpha_{h/v}$  is the beamsplitter reflectance parameter for H/V polarisation and the rows and columns are labelled to make explicit the coupling between the H and V subspaces. We can see that the transformation in Eq. 8 couples different polarisations to different spatial modes (ports) but does not mix the amplitudes of the internal state components. To accomplish this we need birefringent materials. Following the same mode ordering as before, the transformation induced by placing two birefringent plates at the outputs of a beamsplitter may be represented as

$$R = \begin{pmatrix} e^{-i\eta_1/2}(\cos \theta_1^2 + e^{-i\eta_1} \sin \theta_1^2) & 0 & e^{-i\eta_2/2}(\cos \theta_2^2 + e^{-i\eta_2} \sin \theta_2^2) & 0 \\ 0 & e^{-i\eta_2/2}(\cos \theta_2^2 + e^{-i\eta_2} \sin \theta_2^2) & 0 & e^{-i\eta_1/2}(\cos \theta_1^2 + e^{-i\eta_1} \sin \theta_1^2) \\ e^{-i\eta_1/2}(1 - e^{i\eta_1})e^{i\phi_1} \cos \theta_1 \sin \theta_1 & 0 & e^{-i\eta_2/2}(1 - e^{i\eta_2})e^{i\phi_2} \cos \theta_2 \sin \theta_2 & e^{-i\eta_2/2}(1 - e^{i\eta_2})e^{-i\phi_2} \cos \theta_2 \sin \theta_2 \\ 0 & e^{-i\eta_2/2}(1 - e^{i\eta_2})e^{i\phi_2} \cos \theta_2 \sin \theta_2 & 0 & e^{-i\eta_1/2}(1 - e^{i\eta_1})e^{-i\phi_1} \cos \theta_1 \sin \theta_1 \end{pmatrix}, \quad (9)$$

where  $\eta_i$  is the linear retardance,  $\phi_i$  is the circularity and  $\theta_i$  is the waveplate angle. The index,  $i$  denotes the output port of the beamsplitter. The rows and columns denote the same coupling of subspaces as in Eq. 8. We can then create the Givens rotations corresponding to these  $4 \times 4$  matrices by including four superscripts instead of two signifying that eight terms will be replaced in the  $2M \times 2M$  dimensional identity matrix like

$$\lambda^{mp} = g^{m_H, m_V, p_H, p_V}(X), \quad (10)$$

where  $C$  is the  $4 \times 4$  coupling matrix between spatial modes  $m$  and  $p$ . The aggregate transformation of an IPBS followed by two birefringent plates followed by a single phase shifter is then written

$$\lambda^{mp} = g^{m_H, m_V, p_H, p_V}(PS) * g^{m_H, m_V, p_H, p_V}(R) * \dots \dots * g^{m_H, m_V, p_H, p_V}(\text{IPBS}). \quad (11)$$

We can then build the full  $2M \times 2M$  network matrix by

multiplying the  $Z \lambda^{mp}$  matrices according to the crossing point order specified in Eq. 7.

## ENCODING SCHEMES

The first step of operating a machine learning model is to encode data inputs  $\mathbf{x} = (x_1, \dots, x_N)$  in such a way that the device can process it. Encoding data into the PLON is achieved by feeding a fixed, horizontally polarised input state into an encoding layer composed of a quarter- and half-waveplate placed before each input port. To build the scattering matrix of this layer we multiply  $M$  Givens rotations generated by the Jones matrices of the encoding waveplate combination  $J(\theta_{Q,m}(\mathbf{x}), \theta_{H,m}(\mathbf{x}))$ . These rotations act only on the  $2 \times 2$  subspace spanned by the polarisation modes  $(m_H, m_V)$  at each port. Thus the resulting matrices are block diagonal and can be multiplied

in any order.

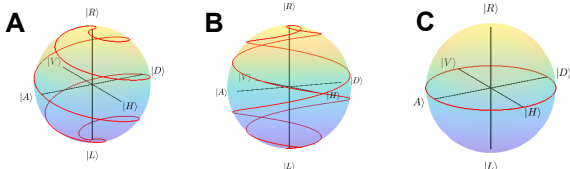
$$E(\mathbf{x}) = \prod_m^M g^{m_H, m_V}(J(\theta_{Q,m}(\mathbf{x}), \theta_{H,m}(\mathbf{x}))) \quad (12)$$

An encoding scheme then is realized by a set of  $2M$  waveplate angles  $(\theta_{Q,m}(\mathbf{x}), \theta_{H,m}(\mathbf{x}))$  which are functions of the data. These functions create states which follow closed trajectories on the Poincare sphere at the corresponding port and the choice of an encoding scheme determines the character of the output functions of the device [? ? ?]. A complete characterization and optimization over possible encodings is beyond the scope of this work, however, we propose a few natural options here and provide some analysis in order to clarify some details of the main text.

All encodings used in this work are classes of closed spirals as shown in Supplementary Figure 2. As such we have unified them with a single parametrization, periodic on the interval  $[-1, 1]$  with degrees of freedom for each port  $m$

$$\begin{aligned} \theta_{Q,m}(\mathbf{x}) &= P_m F_m (1 + 2\mathbf{x} - 4\mathbf{x} G_m \mathcal{H}(\mathbf{x})) \frac{\pi}{4} \\ \theta_{H,m}(\mathbf{x}) &= P_m (\nu_m \mathbf{x} + F_m (G_m \mathcal{H}(\mathbf{x})) \dots \\ &\dots + 2\nu_m \mathbf{x} G_m \mathcal{H}(\mathbf{x}) - 2\nu_m \mathbf{x}) \frac{\pi}{4} \end{aligned} \quad (13)$$

where  $\mathcal{H}(\mathbf{x})$  is the Heaviside step function,  $\nu_m$  determines the number of azimuthal orbits the spiral will complete and  $F_m$  and  $G_m$  are boolean variables which determine if the trajectory leaves the equator and if the spiral reverses direction at the poles to interleave, respectively. The variable  $P_m$  is defined on the continuous interval  $[0, 2]$  and sets the starting point of the encoding such that the polarisation state of ports can traverse their trajectories with different phase offsets. This creates output functions with more phase diversity and increases the performance of fitting.



Supplementary Figure 2. Poincare sphere representations of a single port's polarisation trajectory over the data domain for various encoding schemes. Encodings considered here are: A. interleaved spiral ( $F = 1, G = 1, \nu = 3$ ) B. overlapping spiral ( $F = 1, G = 0, \nu = 3$ ) C. linear ( $F = 0, G = 0, \nu = .5$ ).

## SIMULATION OF INPUT STATES

To simulate and compare input Fock, hybrid and coherent states subject to PNR detection we can express them in a unified form as

$$\begin{aligned} |\psi_{\vec{n}, \vec{\alpha}}\rangle &= \prod_{m=1}^M e^{\alpha_m a_m^\dagger - \alpha_m^* a_m} \frac{(a_m^\dagger)^{n_m}}{\sqrt{n_m!}} |0\rangle \\ &= \prod_{m=1}^M D_m(\alpha_m) \frac{(a_m^\dagger)^{n_m}}{\sqrt{n_m!}} |0\rangle. \end{aligned} \quad (14)$$

Setting the  $\alpha_m = 0$  simplifies Eq 14 to the standard form of a Fock state while setting the  $n_m = 0$  simplifies it to a multimode coherent state. To calculate the amplitudes of different PNR detection results we expand the  $D_m(\alpha_m)$  into the standard Poissonian-weighted power series of creation operators truncated at the order where the coefficient falls below one percent of the peak value. The result is a superposition over Fock states which we propagate through the network individually and recombine into a coherent sum at the output. In the case of polarised states, we apply the operator replacement rule from Section and proceed in the same way. Since we do not consider polarisation in the detection phase, a partial trace is performed over the polarisation degree of freedom after propagating the full state through the network.

## PERFORMANCE MEASURES, NOISE AND SAMPLING

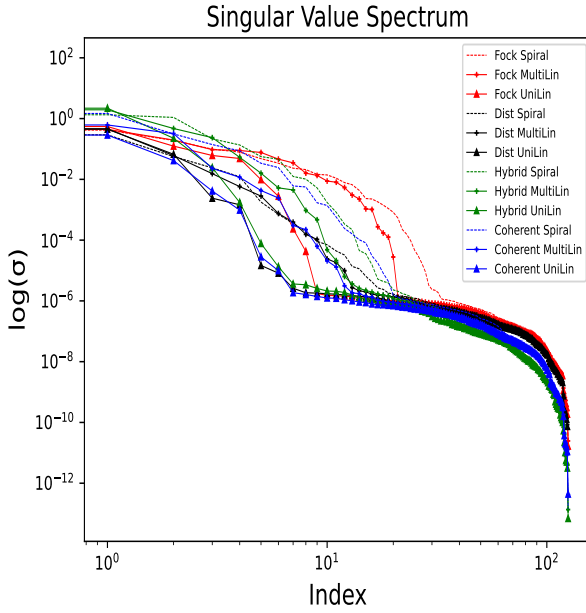
A reservoir and encoding scheme provide a general engine that can process input data and is specialized to a task by the weight matrix. The device performance on any task is determined by the set of linearly independent observable functions it can generate and whether we can accurately approximate their distribution for a given number of samples and a given detector quality. These properties may be gleaned from the output functions generated during training.

### Data matrix rank

During the training phase labeled data is fed into the network and the reservoir output probabilities are stored in an array  $O$ . The Gram matrix  $O^\dagger O$  then is a Hermitian matrix that contains all inner products between output function pairs. By performing a singular value decomposition on this matrix we can determine its spectrum  $\{\sigma_i\}$ . The number of non-zero  $\sigma_i$  gives  $\text{rank}(O^\dagger O)$  which tells us the number of linearly independent functions generated at the output while the magnitude of the singular values tells us their relative frequency.

## Spectral entropy

If it were possible to generate an infinite number of samples with perfect detection, then designs that generated a higher number of singular values would give the best performance. However, in the presence of noise and finite sampling we will only be able to access a subset of singular vectors; those with the highest singular values. The dimension of this subset depends on the number of samples taken and noise parameters, effectively changing the rank of the output. The noise level can be seen in Supplementary Figure 3 as the inflection point in each curve near a y value of  $10^{-6}$ . Beyond the effective rank, functions are poorly sampled and contribute mostly noise. Thus, to distinguish the fitness of different designs under reasonable assumptions of operation, we must consider the distribution of the singular value spectrum.

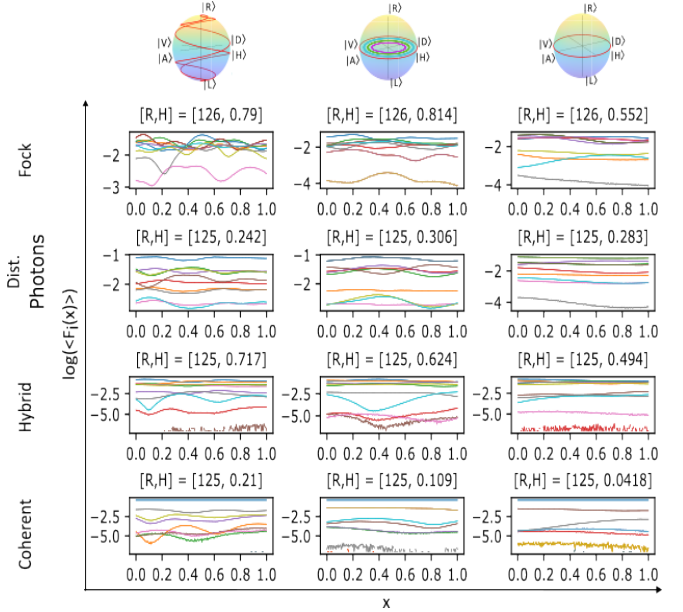


Supplementary Figure 3. Singular value spectra for a combination of states and encodings. Calculated with parameters  $\eta = .9$ ,  $N_{\text{samp}} = 10^7$  and post-selected for detection events of  $\leq 4$  photons. The states used are Fock:  $|1, 1, 1, 1, 0\rangle$ , Distinguishable four photon state:  $|1, 1, 1, 1, 0\rangle$ , Hybrid:  $|\alpha = .5 + 1, \alpha = .5 + 1, 0, 0, 0\rangle$  and Coherent:  $|\alpha = 1.5, \alpha = 1.5, 0, 0, 0\rangle$ . Encodings are Uniform Linear ( $F = 0, G = 0, \nu_m = .5$ ), Multi-Linear ( $F = 0, G = 0, \nu_m = m$ ) and Spiral ( $F = 1, G = 0, \nu_m = 3m$ ).

Because the goal is to resolve the largest number of singular vectors in a given number of samples, a preferred spectrum will approach threshold gradually. Entropy can be applied as a measure of uniformity of a distribution. With this in mind, we define the spectral entropy  $H$ .

$$H = - \sum_i \sigma_i \log_2 \sigma_i. \quad (15)$$

Where  $\{\sigma_i\}$  is the normalized singular value spectrum of the matrix  $O^\dagger O$ . A lower spectral entropy implies that the effective rank of a system will be reduced more rapidly as detector efficiency decreases or fewer samples are taken. Importantly,  $H$  provides a figure of merit that increases with both the number of basis functions and the uniformity of their distribution. This trend of greater bunching of the output functions with larger  $H$  is demonstrated in Supplementary Figure 4. A key observation is the comparatively low entropy of the output function produced by the distinguishable photon state. As the only difference between this state and the Fock state is the presence of multiphoton interference it highlights the importance of the quantum character of the source. Although we can achieve scaling of the output feature space without a quantum source, multiphoton interference grants an advantage through the distribution of the singular value spectrum of the output making it more robust to realistic experimental implementation.



Supplementary Figure 4. Ten most probable output functions for three different states and encodings post-selected for detection events of  $\leq 4$  photons with  $\eta = .9$  and  $N_{\text{samp}} = 10^7$ . The states used are Fock:  $|1, 1, 1, 1, 0\rangle$ , Distinguishable four photon state:  $|1, 1, 1, 1, 0\rangle$ , Hybrid:  $|\alpha = .5 + 1, \alpha = .5 + 1, 0, 0, 0\rangle$  and Coherent:  $|\alpha = 1.5, \alpha = 1.5, 0, 0, 0\rangle$ . Encodings are Uniform Linear ( $F = 0, G = 0, \nu_m = .5$ ), Multi-Linear ( $F = 0, G = 0, \nu_m = m$ ) and Spiral ( $F = 1, G = 0, \nu_m = 3m$ ).

## Noise model

To simulate output measurements under real-world conditions, we need to formulate a model for noise. Assuming perfect sources, noise in a LON can have two sources: losses in the network and imperfections in the detectors. Although network losses can impact the output statistics it is common to neglect them for proof-of-principle simulations. This can be justified on the experimental side as LONs can be manufactured with tolerances such that losses are negligible for modestly sized networks and also for practical reasons as simulation of inhomogenous loss quickly becomes intractable. In this work we focus on the effect of detector imperfections including dark counts and detector losses. We consider the case of one PNR detector at each output port and assume independent noise processes for each. To justify neglecting dark noise in our model we make a conservative estimate of dark noise for a modern single photon detector as 100 cps. Assuming a coincidence window of 10 ns this yields an average of  $(1 \times 10^{-6})^N$  dark counts per N-photon detection event. Although modern detectors can exhibit negligible levels of dark noise even in the case of singles detection, the probability of a spurious detection event rapidly trends towards zero as we consider two-photon events and higher. Detector losses, however, can have a significant impact on the detection process even with high quantum efficiencies. We model the probability of missing  $n_m^{miss}$  out of  $n_m$  photons at a given port as a binomial process

$$P(n_m^{miss}) = \binom{n_m}{n_m^{miss}} (1 - \eta)^{n_m^{miss}} \eta^{n_m - n_m^{miss}} \quad (16)$$

where  $\eta$  is the detector quantum efficiency. This process maps an output N-photon Fock state  $|\vec{n}\rangle$  to a probability distribution over a subspace of Fock states  $|\vec{n}'\rangle$  with probabilities

$$P(\vec{n}'|\vec{n}) = \prod_m P(n_m^{miss}). \quad (17)$$

Once we propagate an input state through the network for the ideal case we then apply the binomial loss model to redistribute the probabilities over the  $N' = N - \sum_m n_m^{miss}$  Fock subspace.

## Considerations on comparing states

There are few degrees of freedom in a pure Fock state, but hybrid and coherent states are characterized by a set of continuous amplitudes  $\alpha_m$ . Fair comparison of the performance of these three classes of states on a task presents a challenge as they have inherently different character. For instance, if we post select on events which contain four or less photons we can make a choice of amplitudes

that maximizes the probability mass in this subspace. However, a given target function may contain a Fourier spectrum which overlaps more with frequencies generated by three-photon events. This makes the choice of optimal  $\alpha_m$  task-specific rather than just depending on the post-selected subspace. In addition, detector losses couple higher to lower photon number states which shifts the probability mass and must be accounted for. We can then treat the  $\alpha_m$  as hyper-parameters which may be chosen based on the task at hand. In the main body, we have chosen to keep the problem as general as possible and set the  $\alpha_m$  to maximize probability mass in the post-selected subspace rather than go through this process of specialization.